J Mater Sci (2016) 51:2926–2934
DOI 10.1007/s10853-015-9601-0

Modelling grain boundary sliding during creep of austenitic stainless steels

Junjing He[1] · Rolf Sandström[1]

Received: 18 September 2015 / Accepted: 16 November 2015 / Published online: 23 November 2015
© Springer Science+Business Media New York 2015

Abstract Two models are presented for grain boundary sliding (GBS) displacement during creep. GBS is considered as crucial for the formation of creep cavities. In the first model, the shear sliding model, GBS is accommodated by grains freely sliding along the boundaries in a power-law creeping material. The GBS rate is proportional to the grain size. In the second model, the shear crack model, the sliding boundaries are represented by shear cracks. The GBS rate is controlled by particles in the boundaries. In both models, the GBS displacement rate is proportional to the creep strain rate. Both models are consistent with existing experimental observations for GBS during creep of austenitic stainless steels. For cavity nucleation at particles, Harris' model (1965) for the relationship between GBS and a critical particle size has been analysed and found to be in agreement with observations.

Introduction

There is an urgent demand to increase the operating temperature and stress in power plants [1] in order to reduce the CO_2 emission and other environment pollution, as well as save costs. However, the life of components such as boiler tubes, in high temperature and stress conditions is limited by the properties of the materials, especially creep strength and oxidation resistance. Austenitic stainless steels are widely used for the high-temperature components of power plants. Therefore, it is of utmost importance to understand the life controlling rupture mechanisms in these steels.

During creep deformation in metals, a relative movement of grains along the grain boundaries takes place, which is referred to as grain boundary sliding (GBS). The sliding has two main effects. It increases the overall creep rate and gives rise to nucleation of creep cavities. For a homogeneous grain structure, Crossman and Ashby [2] and Ghahremani [3] modelled the GBS accommodated by a plastic flow field within the grains, which is generally observed above 0.3 T_m (where T_m is the melting temperature). In their models, the grain boundary was assumed to be a layer that slides in a Newtonian viscous way due to shear stresses in its plane. They found that the fractional contribution of GBS to the total displacement rate was only dependent on the stress exponent. GBS is accommodated by elastic, plastic and diffusive flow of matter [2, 4], and can contribute significantly to the total creep strain. Up to 30 % increases in the creep rate was predicted [2, 3]. Riedel [5] suggested that the applied shear stress is partly supported by grain boundary particles and triple grain junctions in a polycrystal. He developed a model for GBS, where the boundaries were represented by shear cracks.

The second effect of GBS is the formation of creep cavities. Creep cavitation is one main reason for the failure of materials at high temperatures. Creep rupture is often caused by the formation, growth and coalescence of creep cavities along grain boundaries. Creep cavities typically nucleate at grain boundaries, which are associated with GBS [6–9]. The cavity nucleation takes place at inclusions or second-phase particles, as well as at ledges and other irregularities, like grain boundary triple points or sub-boundary/grain boundary intersections [10]. A large

✉ Junjing He
junjing@kth.se

Rolf Sandström
rsand@kth.se

[1] Materials Science and Engineering, KTH Royal Institute of Technology, 100 44 Stockholm, Sweden

volume of research effort has been performed to explore the mechanisms of cavity nucleation. Raj et al. [11, 12] used classical nucleation theory to describe how cavities could be formed at grain boundaries by clustering of vacancies. This model results in a threshold stress [11] below which the nucleation will never occur and an incubation time [12] which indicates that the stress concentration must be maintained until the steady-state nucleation rate has been reached. However, as demonstrated by Yoo and Trinkaus [13], Dyson [14] and Riedel [5], the relaxation times of the stress concentrations are shorter than the incubation times for cavity nucleation, and the stresses required for cavity nucleation are orders of magnitude higher than the applied stresses at which nucleation actually occurs.

Harris [15, 16] suggested that particles can act as cavity nuclei if the GBS rate exceeds the longitudinal sintering rate and if intersecting slip spreads the cavity laterally faster than axial sintering. Harris [16] concluded that for smaller particles to initiate cavities, a higher GBS displacement rate is required. However, this theory has been ignored because of the difficulty to calculate the GBS rate [17]. For cavity nucleation at substructures, a model has been proposed by Sandström et al. [10, 18] that cavities are generated when the particles or subboundary corners on one side of a sliding grain boundary meet the subboundaries on the other side of the sliding grain boundary.

In this paper, models for GBS will be presented and compared to the experimental data. Then a relationship between GBS and cavity nucleation will be introduced which involves nucleation at particles. It provides further possibilities of verifying the GBS models. In the forthcoming paper [18], cavity nucleation at substructures that is related to GBS will be presented.

Characterization of GBS

Shear sliding model

Although there are still many different views about the mechanisms of cavity nucleation, it is well accepted that GBS plays an important role for nucleation at particles or subboundaries. It has been known for a long time that the amount of GBS is closely related to the creep strain [19]. Crossman and Ashby [2] and Ghahremani [3] performed FEM-analysis on a homogeneous set of hexagonal grains exposed to power-law creep. From their work a quantitative expression for the amount of GBS can be derived. This derivation of GBS is referred to as the shear sliding model here. The shear behaviour of grain boundaries was described with the help of their intrinsic viscosity η_{int}

$$\eta_{\text{int}} = \frac{k_{\text{B}}T}{8bD_{\text{GB}}}, \tag{1}$$

where k_{B} is Boltzmann's constant, T the absolute temperature, b Burgers' vector and D_{GB} the grain boundary diffusion coefficient. The rate of GBS can be expressed as

$$v_{\text{sd}} = \frac{\delta}{\eta_{\text{int}}}\tau, \tag{2}$$

where δ is the grain boundary width and τ is the shear stress. Equation (2) gives such high sliding rates in relation to the deformation due to the power-law creep in the grain interiors that the grain boundaries can be assumed to slide freely. Thus, at normal creep rates, the resistance to deformation of the grain boundaries is much lower compared to that of the grains. Therefore, the grain boundaries can be considered as flaws in the materials. In this case, the influence of GBS on the total creep rate can be represented by a stress enhancement factor f. Then, the overall creep rate $\dot{\varepsilon}$ that takes the influence of GBS into account is [2, 3]

$$\dot{\varepsilon} = \dot{\varepsilon}_0\left(f\frac{\sigma}{\sigma_0}\right)^n, \tag{3}$$

where σ is the applied stress, and $\dot{\varepsilon}_0$, n, σ_0 are constants in the Norton equation. The fractional contribution Φ of GBS displacement rate v_{sd} to the total displacement rate v_{tot} can be expressed as

$$\Phi = \frac{v_{\text{sd}}}{v_{\text{tot}}}. \tag{4}$$

The Φ value was found to be dependent only on the stress exponent n. The value of Φ is in the range from 0.1 to 0.33 when the stress exponent n varies from 1 to infinity. Values from [3] are used since tensile stresses were applied in the modelling rather than the shear stresses in [2]. The total displacement rate v_{tot} can be obtained by relating it to the creep rate:

$$v_{\text{tot}} = \frac{3}{2}\frac{d_{\text{grain}}}{\xi}\dot{\varepsilon}, \tag{5}$$

where the factor 3/2 is a result of how the v_{tot} is obtained in the studied grain structure. In the characterization of the percentage of the grain boundary sliding, a hexagonal grain structure was used. A factor ξ is introduced in order to relate the side of the hexagonal grains a_{hex} to the measured grain size d_{grain}. For the area equivalent grain size d_{grain}, the value of ξ is 1.82 [20]. Combining Eqs. (4) and (5), one can get the GBS rate v_{sd}

$$v_{\text{sd}} = \Phi\frac{3}{2}\frac{d_{\text{grain}}}{\xi}\dot{\varepsilon} = C_s(\varepsilon)\dot{\varepsilon}. \tag{6}$$

Equation (6) demonstrates that the GBS rate is proportional to the creep rate and to the grain size of the material.

As will be discussed in "Modelling results" section, experimentally the amount of GBS is approximately proportional to the creep strain. So the GBS rate can be related to the creep rate by a parameter $C_s(\varepsilon)$, which is slightly strain dependent. Using the information in [4], it is possible to show that Eq. (6) is also valid when diffusion creep controls the bulk deformation, provided the same type of assumption about a homogenous grain structure is made. For austenitic stainless steels, the typical creep exponent n is in the range of 5–10, and the corresponding Φ value is about 0.23 [3]. The modelling results will be shown and compared to the experimental observations in "GBS displacement" section.

Shear crack model

Riedel [5] developed a model where a sliding grain boundary was described as a shear crack. In this shear crack model, constraints on GBS were considered. The model involved Newtonian viscous grain boundaries between hexagonal, power-law creeping grains, which showed agreement with finite element calculations.

A shear crack of length $2a$ (a is half the grain facet size) was subjected to a remote stress system σ_{ij}^{∞} and to shear tractions τ_b across the grain boundary. The average GBS displacement rate v_{sd} across the crack was found to be

$$v_{sd} = \frac{3\pi}{4}\frac{1}{\sqrt{na}}\frac{\dot{\varepsilon}_e}{\sigma_e}\left(\sigma_{12}^{\infty} - \tau_b\right), \tag{7}$$

where σ_{12}^{∞} is the applied resolved shear stress on the boundary, n is the creep exponent, $\dot{\varepsilon}_e = B\sigma_e^n$ is the creep rate, σ_e is the remotely applied equivalent tensile stress. For a hexagonal array of grains under plane strain tension $\sigma_{12}^{\infty}/\sigma_e = 1/2$.

Riedel modelled the power-law creep around particles in the grain boundary. It was assumed that the particles were flat and well separated with a diameter p. This gave the GBS displacement rate v_{sd}

$$v_{sd} = \frac{9}{4}\frac{1}{\sqrt{1+\frac{3}{n}}}\frac{\tau_b}{\sigma_e}\frac{\lambda^2}{p}\dot{\varepsilon}_e = C_s\dot{\varepsilon}_e, \tag{8}$$

where λ is the particle spacing. The sliding rate by power-law creep around particles must be equal to the sliding rate calculated across the shear cracks. Thus, by assuming that the sliding rates in Eqs. (7) and (8) are the same, one can get the shear stress τ_b across the boundary.

$$\frac{\tau_b}{\sigma_e} = 1/\left(\frac{3}{\sqrt{1+3/n}}\frac{\lambda^2}{pd_{grain}\pi\sqrt{n}} + 1\right) \tag{9}$$

Equation (9) is inserted into Eq. (8) to obtain the final sliding rate. The results depend on the particle spacing and particle diameter. For the calculation of the C_s value, the particle dimensions will be obtained from both experimental data and computations, see "Particle spacing and dimensions" section.

Experimental measurements of GBS

The modelling results of the relationship between GBS displacement and creep strain are compared with the experimental results in "Modelling results" section. GBS displacements can be measured in a number of different ways, which has to be taken into account when comparing with the model results. Figure 1 illustrates the common way of defining the GBS displacement and its components [21–24]. The GBS displacement of this bicrystal (grain 1 and grain 2) is

$$\mu = \frac{\omega}{\tan\theta} + \frac{v}{\tan\varphi}, \tag{10}$$

where μ is the component along the stress axis, ω, the transverse component, is the component perpendicular to the stress axis and in the plane of the specimen surface. ν, the vertical component, is the component perpendicular to the stress axis and the specimen surface. θ is the angle between the surface trace of the boundary and the stress axis, and φ is the angle between the boundary and the surface on a longitudinal section cut perpendicular to the surface. For the specimen interior, the two terms in Eq. (10) can be taken as equal, while at surfaces, they might be slightly different. As proved by Gates and Stevens [23] the two angles are approximately equal, $\theta \approx \varphi \approx 1.2$ rad. ω and ν can be taken as equal in the grains, so one can get a simplified result for GBS displacement:

$$\mu = \frac{2\omega}{\tan\theta} = \frac{2v}{\tan\varphi} \tag{11}$$

In [22], the GBS displacement is taken as the square root of quadratic sum of the components ω and v, $\mu' = \sqrt{\omega^2 + v^2}$, which has been transferred to the components along the stress axis. In the references considered for

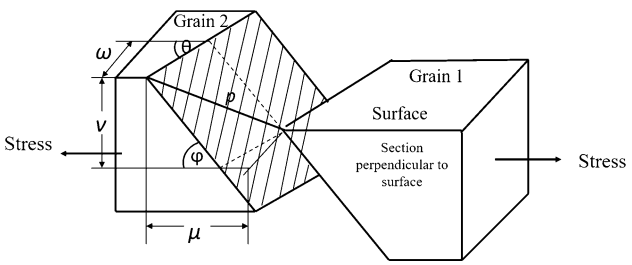

Fig. 1 Components of grain boundary sliding vector, p during creep (redrawn after [21–24])

experimental data, different components have been used, as listed in Table 1. In order to unify them, we transferred all GBS data to the one along stress axis μ with the aid of Eq. (11).

Relation between GBS and cavity nucleation at particles

Critical particle radius

For cavity nucleation at particles, a critical radius seems to exist [6–9, 21]. The particles must have a minimum size to induce cavity nucleation. Harris [15, 16] suggested a model which relates the critical particle size to the GBS displacement rate. This model provides an additional possibility for comparing the GBS models with experimental data. Harris assumed that particles will not be able to prevent GBS if stress-induced self-diffusion is fast enough to relax the stress concentrations. Under the same conditions cavity nucleation will not be initiated. In his model, a cubic particle with side l appears in a sliding grain boundary with a stress differential across the particle equal to the macroscopic shear stress σ_s. The stress-induced flux of matrix atoms from the compressed faces across the particle surface is $2\sigma_s\delta D_{GB}\Omega/(k_BT)$, where δ is the thickness of the grain boundary and Ω is the atomic volume. Then the relative sliding rate of grains due to vacancy transport is $2\sigma_s\delta D_{GB}\Omega/(k_BT)/l^2$. The condition for stress concentration at particle is

$$v_{sdc} > \frac{2\delta D_{GB}\Omega}{l^2 k_B T}, \tag{12}$$

where v_{sdc} is the critical GBS velocity. If the condition in Eq. (12) is satisfied, the particle can act as an obstacle to GBS and initiate cavity nucleation. By considering the equilibrium concentration of vacancies in a grain boundary and near the cavity surface, the final critical condition for cavity formation is

$$v_{sdc} = \frac{\delta D_{GB}}{r_p^2 \ln\frac{\lambda}{2r_p}}\left(\exp\frac{2\gamma_s\Omega}{k_B T r_p} - 1\right), \tag{13}$$

where γ_s is the free surface energy and r_p is the particle radius. The radius of the diffusion field of atoms to the cavity is taken as half the interparticle spacing $\lambda/2$. For particles smaller than r_p, a higher GBS velocity v_{sdc} is required. The critical particle radius can be obtained if the GBS rate is known from the models described above. The critical radius from Harris' model will be compared with experimental observations in "Modelling results" section.

Particle spacing and dimensions

In Riedel's model for GBS, Eq. (8) and Harris' model for the critical particle radius, Eq. (13), the average particle size and inter particle spacing are needed. In some cases experimental information is available. However, in other cases, particle parameters have to be estimated. This can be done with commercial software that provides thermodynamic modelling of particle nucleation and growth. In our case, MatCalc has been used [27].

For calculation of the formation of particles with MatCalc, the setup of the calculation system is described as follows:

(1) The databases mc_fe_v2009.tdb (phase chemistry) and mc_fe_v2.001.ddb (diffusion coefficients) were used. The chemical composition was taken from the different references in order to compare the results with the experimental ones. The austenitic stainless steels that were analysed are listed in Table 2.
(2) $M_{23}C_6$ was considered as the main particle contributing to the cavity nucleation due to GBS, since it is the main particle observed in the references. The nucleation sites for $M_{23}C_6$ were taken as the grain boundaries in agreement with observations [30].
(3) The precipitation kinetics were calculated at the temperatures in the experiments, which was in the range of 550–812 °C. The isothermal simulation time was set to the testing times as listed in Table 2.

Table 1 Materials for measurement of GBS

Materials	Temperature (°C)	Stress (MPa)	Strain range (%)	Given GBS components	Unify method	Reference
TP347XX	750	78	4–12	Transverse component ω	Eq. (11)	[21]
TP321	650	157–196	0.16–6.19	$\sqrt{\omega^2+v^2}$	Eq. (11)	[22]
TP316	800	36	2–2.12	Component along stress axis μ	μ directly	[23]
20Cr–25Ni	750	62	5–30	Vertical component v	Eq. (11)	[25]
TP316	625	220	34–68	Component along stress axis μ	μ directly	[26]

Table 2 Experimental conditions for comparison to MatCalc calculations

Materials	Temperature (°C)	Stress (MPa)	Test time (hour)	Grain size (μm)	Reference
TP304	727	100	250	90	[6]
18Cr–9Ni	700, 800	65–130	600	22	[7]
TP347XX	750	78	460–5100	65	[8, 21]
TP321	812	49.6	66	30	[28]
TP347	550, 650	123–338	2170	12	[29]

The MatCalc calculations gave the number of particles and their corresponding radii. However, in some cases, the MatCalc results showed particle radii in a narrow range. Then a reference state of particles with an average radius $\overline{r}$ and number of particles N^0_{part} was obtained first. Then, the number of precipitates with radius r_{p} was determined [31]:

$$N_{\text{part}} = N^0_{\text{part}} e^{-(k_{\text{r}} r_{\text{p}} - \delta_{\text{c}})}, \tag{14}$$

where $k_{\text{r}} = 1/\overline{r}$, and $\overline{r}$ is the average particle radius with a corresponding number of precipitates N^0_{part}. For $\delta_{\text{c}} = 1$, N_{part} is the number of particles with radius r_{p}; for $\delta_{\text{c}} = 0$, N_{part} is the number of particles with radius larger than the critical particle radius r_{p}. The particle spacing λ can be obtained in the following way:

$$\lambda = \frac{1}{\sqrt{N_{\text{part}}}} \tag{15}$$

In the MatCalc calculations, five reference state points were used to calculate the average values.

Modelling results

Constants used in the model

The constants used in the computations are shown in Table 3.

Results of precipitation calculation

Particle spacing and number density were calculated with MatCalc for the conditions in Table 2. The particle radii along grain boundaries were in the range of 0.2–1 μm from the experimental observations. The particle spacing obtained from MatCalc are compared with the experimental observations [7, 21] in Fig. 2. The MatCalc calculations show an order of magnitude agreement with the experimental values. The average value of the ratio λ/r_{p} obtained from MatCalc is about 7, Fig. 2. MatCalc predictions for precipitation in austenitic stainless steels have also been verified elsewhere, see for example [37, 38].

GBS displacement

Figure 3 shows the comparison of the shear sliding model, Eq. (6), and experimental GBS displacement as a function of creep strain. The grain size in Eq. (6) was taken directly from the experimental sources. For most cases, the modelling results is within a factor of two from the experimental data. One exception is the case for TP316 [26] with large strains and grain size (450 μm). This deviation will be analysed in the discussion.

In Fig. 4, the average experimental and model values are compared. The average C_{s} value of the shear sliding model (11 μm) was calculated based on the experimental grain size from [21, 22, 25] (without the case [26] with large grain size). In the other model, the shear crack model, Eq. (8), C_{s} is related to the particle spacing and diameter. Since the detailed particle distributions cannot be assessed from the experimental sources, a precise comparison cannot be made. Instead, the expected particle distributions have been computed with the help of the MatCalc results. From both experimental observations [7, 21] and modelling results for particles radius and spacing, the value of $\tau_{\text{b}}/\sigma_{\text{e}} \approx 0.45$ can be determined from Eq. (9). Finally the C_{s} value can be obtained from Eq. (8). The average value is

Table 3 Constants for austenitic stainless steels used in the computations

Parameter description	Parameter	Value	Reference
Grain boundary diffusion coefficient	δD_{GB}	$10^{-9.87} e^{\frac{-2.187e5}{R_{\text{gas}} T}}$ m^3 s^{-1}	[32]
Atomic volume	Ω	1.21×10^{-29} m^3	[33]
Boltzmann constant	k_{B}	1.381×10^{-23} J K^{-1}	
Creep exponent	n	5	[34]
Burgers vector	b	2.58×10^{-10} m	
Surface free energy per unit area	γ_{s}	2.8 J m^{-2}	[35]
Poisson's ratio	ν	0.3	[36]

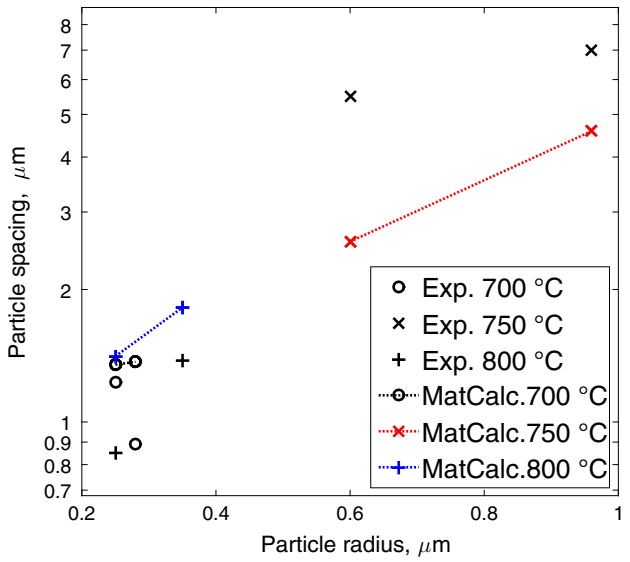

Fig. 2 Comparison of MatCalc and experimental particle spacing versus particle radius. Experimental data for 18Cr–9Ni from Shin et al. [7] and for TP347XX from Laha et al. [21]

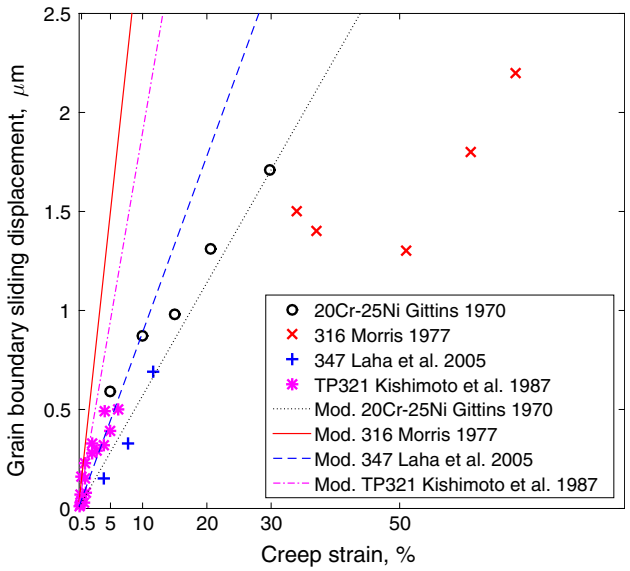

Fig. 3 Comparison of the shear sliding model and experimental GBS displacement as a function of creep strain for different types of austenitic stainless steels. Shear sliding model, Eq. (6); experimental data from [21, 22, 25, 26]

4.3 μm based on the modelling results with particle radii in the range of 0.2–1 μm.

The two models (shear sliding and shear crack models) are compared with the experimental GBS displacement in Fig. 4. The experimental data are from [21–23, 25, 26] for different types of austenitic stainless steels, see Table 2. The grain size is not given in [23]. For this reason this reference was not included in Fig. 3. In Fig. 4, Exp. Ave.

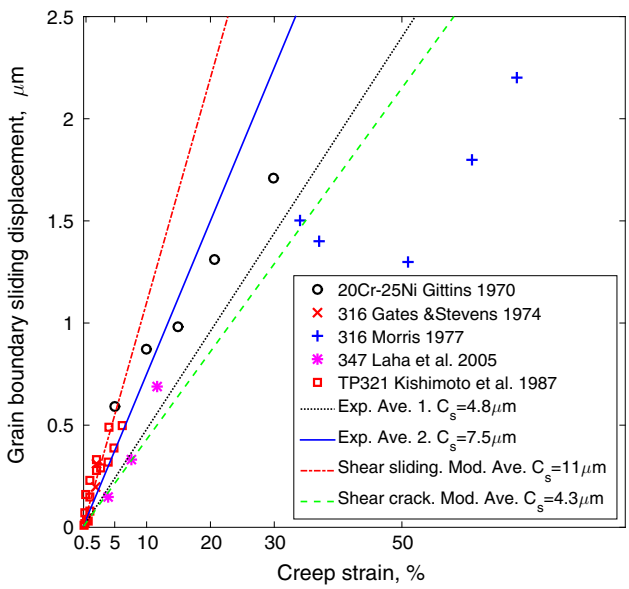

Fig. 4 Modelling and experimental GBS displacement as a function of creep strain for different types of austenitic stainless steels. Experimental data from [21–23, 25, 26]

1., is the experimental average value of C_s, which is obtained by regressing all experimental data. Exp. Ave. 2. is the experimental average value without considering the case [26] with very large creep strain and grain size. From Fig. 4, it can be readily seen that, the averages of the shear sliding model and the experiments are within a factor of two (C_s = 11 and 7.5 μm respectively). The shear crack model gives a lower value for C_s (4.3 μm). Since the shear crack model is only weakly grain size dependent there is no longer any reason to exclude Ref. [26] and then the experimental average is 4.8 μm.

Cavity nucleation at particles

For creep cavity nucleation at particles, Eq. (13) gives a critical particle radius (particles larger than this would nucleate cavities), which can be related to the GBS velocity. The critical particle radius can be obtained by combining Eq. (13) with the GBS models, Eq. (6). In Eq. (13) the average value of the ratio λ/r_p is about 7 as obtained from Fig. 2. The modelling critical particle radius for cavity nucleation is compared with the experimental observations in Fig. 5. The GBS velocity is plotted as a function of the critical particle radius at different temperatures for different types of austenitic stainless steels [6–8, 21, 28]. The experimental conditions are listed in Table 2. In Eq. (6), the grain size and creep rate are taken from the experimental references. The experimental critical particle radius is taken as the minimum particles that nucleated

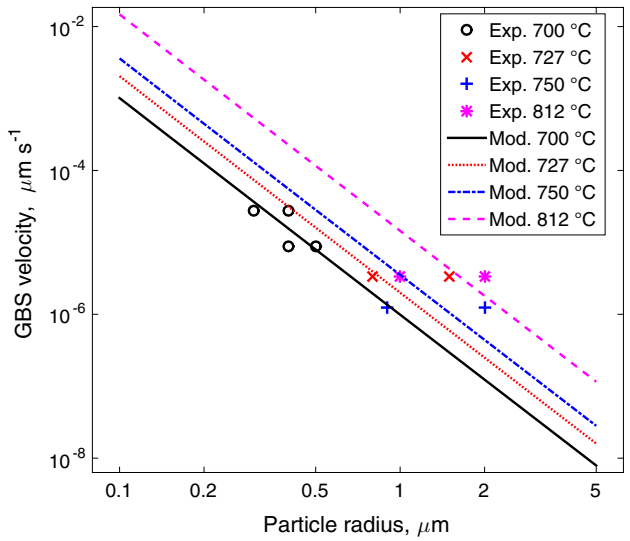

Fig. 5 Comparison of experimental and modelling GBS velocity as a function of particle radius. Experimental data for 18Cr–9Ni from Shin et al. [7], for TP347XX from Laha et al. [8, 21], for TP304 from Hong et al. [6] and for TP321 from Arzate [28]. Modelling results from Eq. (13)

cavities. The modelling results are consistent with the experimental ones.

After determining the critical particle radius, the number of precipitates can be obtained from MatCalc calculations. It is assumed that particles that are larger than the critical size will nucleate cavities. The resulting estimated number of cavities is compared with the observed ones in Fig. 6. The experimental data is from [7, 8, 21, 28, 29] for different types of austenitic stainless steels, the conditions of which are listed in Table 2. The experimental number of cavities is in general in a range. For TP347XX [8, 21], the experimental number of cavities is in a range from 0.002 to 0.14 μm^{-2}. The modelled number of cavities is of the same order with the experimental ones. The results indicate that the critical particle model can give an order of magnitude estimate of the number of cavities.

Discussion

The accuracy of the GBS models

The validity of the shear sliding model has been demonstrated above for austenitic stainless steels. In a separate publication this has also been shown for copper [39].

The shear sliding and the shear crack models presented in "Shear sliding model" and "Shear crack model" sections give an amount of GBS that is proportional to the creep strain. As shown in Fig. 4, this is in general in good accordance with the experiments. However, the GBS displacement is not always fully linear with the creep strain. As observed by Gittins [25], there can be an initial stage where the GBS displacement rate is larger than that in the following stage. Similar observations have been made by Kishimoto et al. [22] for smaller strains (<10 %). As can be seen there is a gradual decrease in the slope of the curves with increasing strain. However, as shown in Fig. 7, the average value of C_s that relates GBS to the creep rate, can fit the experimental data in a reasonable way. So the deviation from the linear behaviour will not affect the

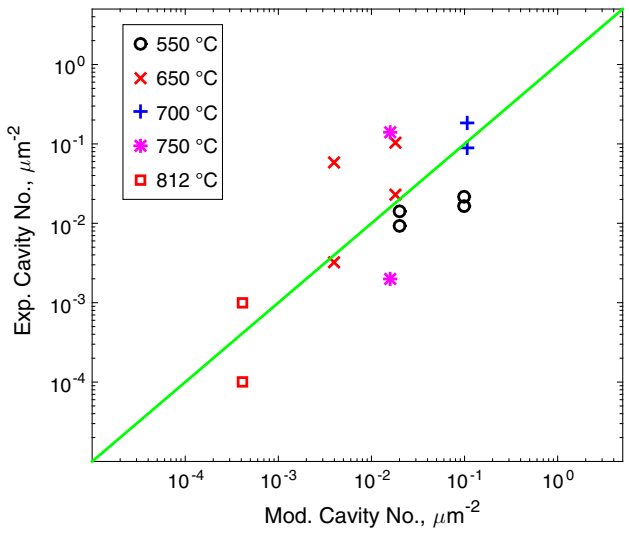

Fig. 6 Comparison of experimental number of cavities and modelling number of particles that initiate cavities. Experimental data for 18Cr–9Ni from Shin et al. [7], for TP347XX from Laha et al. [8, 21], for TP321 from Arzate [28] and for TP347 from Needham and Gladman [29]

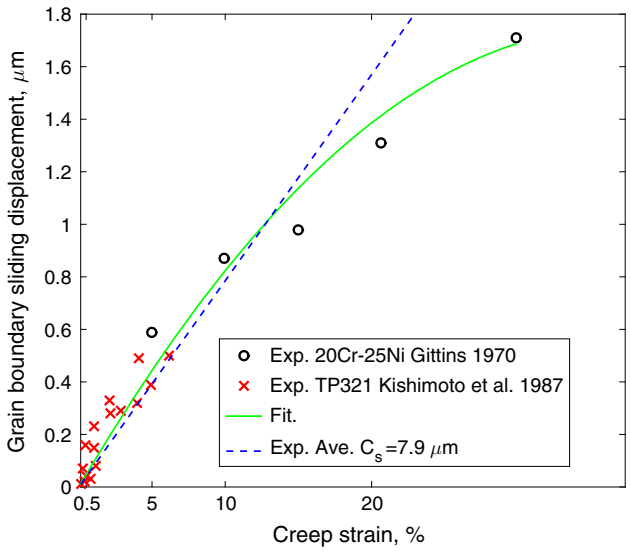

Fig. 7 Experimental GBS displacement as a function of creep strain. Experimental data for 20Cr–25Ni from Gittins [25] and for TP321 from Kishimoto et al. [22]

general relationship between GBS rate and creep rate significantly, which can also be seen in Fig. 4 with combinations of all experimental data. A significant strain dependence of C_s has also been observed for Cu [39].

In the shear sliding model, the displacement is proportional to the grain size, Eq. (6). Most experiments follow this behaviour as is indirectly evident from Fig. 4. There is one noticeable exception. Morris found that GBS for TP316 was virtually independent of grain size for large grain sizes [26]. A large grain size can make GBS difficult because the large grains can lock each other, in particular if the grain structure is inhomogeneous. It should be recalled that the FEM models are using homogenous distributions consisting of grains of only one size. That the shear sliding model tends to exaggerate GBS for large grain sizes has also been observed for Cu [39].

The shear sliding model is based on the general plastic deformation of the grain structure during creep. For the shear crack model, the starting point is the distribution of precipitates in the grain boundaries. According to the model, fine particles should give a low displacement rate and vice versa. A fine particle distribution would reduce the GBS rate. However, there is not sufficient data to directly confirm that by the experiments, except possibly for large grain sizes.

Cavity nucleation at particles

Harris [16] suggested that a critical particle radius exists for cavity nucleation at particles. The critical particle radius is related to the GBS velocity. With the help of the GBS models it is possible to test Harris' approach. The GBS rate is dependent on the grain size and the creep rate, Eq. (6). A higher GBS velocity is required for smaller particle radii to nucleate cavities. For a given GBS rate, only particles with a radius larger than the critical particle radius can nucleate cavities. The model predictions lie in the centre of the experimental data for the number of cavities, Fig. 6. These results clearly support Harris' model for nucleation around particles.

Conclusions

1. Two models for grain boundary sliding (GBS) during creep are presented. The first model, the shear sliding model, is based on previously performed FEM computations of a creeping solid with freely sliding grain boundaries. In the second model, the sliding grain boundaries are considered as shearing cracks. This model referred to as the shear crack model, was originally proposed by Riedel.
2. Both the shear sliding and the shear crack models give a GBS rate that is proportional to the creep rate. The proportionality constant C_s in the two models is at least in qualitative accordance with the experimental data.
3. Harris developed models for cavity nucleation at particles. A critical particle radius must be exceeded for nucleation to take place and this model is related to the GBS velocity. With models available for GBS, it has been possible to compare Harris' model with experiments. The modelling results for the critical particle radius are in agreement with the experimental observations. The number of particles that can initiate cavities is of the same order as the experimental number of cavities.

Acknowledgements Financial support by the European Union (directorate-general for energy), within the project MACPLUS (ENER/FP7EN/249809/MACPLUS) in the framework of the Clean Coal Technologies is gratefully acknowledged. The authors would like to thank the China Scholarship Council (CSC) for funding a stipend (File No. 201207090009) for Junjing He.

Compliance with ethical standards

Conflict of Interest The authors declare that they have no conflict of interest.

References

1. Chai G, Boström M, Olaison M, Forsberg U (2013) Creep and LCF behaviors of newly developed advanced heat resistant austenitic stainless steel for A-USC. Procedia Eng 55:232–239. doi:10.1016/j.proeng.2013.03.248
2. Crossman FW, Ashby MF (1975) The non-uniform flow of polycrystals by grain-boundary sliding accommodated by power-law creep. Acta Metall 23(4):425–440. doi:10.1016/0001-6160(75)90082-6
3. Ghahremani F (1980) Effect of grain boundary sliding on steady creep of polycrystals. Int J Solids Struct 16(9):847–862. doi:10.1016/0020-7683(80)90053-0
4. Raj R, Ashby MF (1971) On grain boundary sliding and diffusional creep. Metall Trans 2(4):1113–1127
5. Riedel H (1984) Cavity nucleation at particles on sliding grain boundaries. A shear crack model for grain boundary sliding in creeping polycrystals. Acta Metall 32(3):313–321
6. Hong JH, Nam SW, Choi SP (1986) The influences of sulphur and phosphorus additions on the creep cavitation characteristics in type 304 stainless steels. J Mater Sci 21(11):3966–3976
7. Shin JK, Nam SW, Lee SC (2005) A study of nitrogen effect on the characteristics of creep-rupture in 18Cr-9Ni austenitic steels. Key Eng Mater 297-300(I):409–414
8. Laha K, Kyono J, Shinya N (2012) Copper, boron, and cerium additions in type 347 austenitic steel to improve creep rupture strength. Metall Mater Trans A 43(4):1187–1197
9. Cui Y, Sauzay M, Caes C, Bonnaillie P, Arnal B (2014) Modeling and experimental study of long term creep damage in austenitic stainless steels. Procedia Mater Sci 3:122–128. doi:10.1016/j.mspro.2014.06.023
10. Sandström R, Wu R (2013) Influence of phosphorus on the creep ductility of copper. J Nucl Mater 441(1–3):364–371. doi:10.1016/j.jnucmat.2013.06.020

11. Raj R, Ashby MF (1975) Intergranular fracture at elevated temperature. Acta Metall 23(6):653–666. doi:10.1016/0001-6160(75)90047-4
12. Raj R (1978) Nucleation of cavities at second phase particles in grain boundaries. Acta Metall 26(6):995–1006. doi:10.1016/0001-6160(78)90050-0
13. Yoo MH, Trinkaus H (1983) Crack and cavity nucleation at interfaces during creep. Metall Trans A 14(3):547–561. doi:10.1007/BF02643772
14. Dyson BF (1983) Continuous cavity nucleation and creep fracture. Scripta Mater 17:31–37
15. Harris JE (1965) An analysis of creep ductility of magnox Al80 and its implications. J Nucl Mater 15(3):201–207
16. Harris JE (1965) Nucleation of creep cavities in magnesium. Trans Metall Soc AIME 233:1509
17. Jiang XG, Earthman JC, Mohamed FA (1994) Cavitation and cavity-induced fracture during superplastic deformation. J Mater Sci 29(21):5499–5514. doi:10.1007/BF00349941
18. He J, Sandström R (2015) Formation of creep cavities in austenitic stainless steels (in press)
19. McLean D, Farmer MH (1957) The relation during creep between grain-boundary sliding, sub-crystal size, and extension. J Inst Met 85(8):41–50
20. Zhang J, Luévano AJ, Przystupa MA (1994) Microstructural models for quantitative analysis of grains and second-phase particles. Mater Charact 33(2):175–185. doi:10.1016/1044-5803(94)90081-7
21. Laha K, Kyono J, Sasaki T, Kishimoto S, Shinya N (2005) Improved creep strength and creep ductility of type 347 austenitic stainless steel through the self-healing effect of boron for creep cavitation. Metall Mater Trans A 36A:399–409
22. Kishimoto S, Shinya N, Tanaka H (1987) Grain boundary sliding and surface cracking during creep of 321 stainless steel. Materials 37(414):289–294
23. Gates RS, Stevens RN (1974) The measurement of grain boundary sliding in polycrystals. Metall Trans 5:505–510
24. Langdon TG (1972) The effect of surface configuration on grain boundary sliding. Metall Trans 3:797–801
25. Gittins A (1970) The kinetics of cavity growth in 20Cr/25Ni stainless steel. J Mater Sci 5:223–232. doi:10.1007/BF00550998
26. Morris DG, Harries DR (1977) Wedge crack nucleation in Type 316 stainless steel. J Mater Sci 12:1587–1597. doi:10.1007/BF00542809
27. Kozeschnik E, Svoboda J, Fischer FD (2004) Modified evolution equations for the precipitation kinetics of complex phases in multi-component systems. Calphad 28(4):379–382. doi:10.1016/j.calphad.2004.11.003
28. Arzate OR, Martinez L (1988) Creep cavitation in type 321 stainless steel. Mater Sci Eng A 101:1–6
29. Needham NG, Gladman T (1980) Nucleation and growth of creep cavities in a type 347 steel. Met Sci 14(2):64–72
30. Farooq M (2013) Strengthening and degradation mechanisms in austenitic stainless steels at elevated temperature. KTH Royal Institute of Technology, Stockholm
31. Sandström R, Farooq M, Zurek J (2013) Basic creep models for 25Cr20NiNbN austenitic stainless steels. Mater Res Innov 17(5):355–359
32. Čermák J (1991) Grain boundary self-diffusion of 51Cr and 59Fe in austenitic NiFeCr alloys. Mater Sci Eng A 148(2):279–287
33. Arai M, Ogata T, Nitta A (1996) Continuous observation of cavity growth and coalescence by creep-fatigue tests in SEM. Jpn Soc Mech Eng 39(3):382–388
34. NIMS creep data sheet for austenitic stainless steels. http://smds.nims.go.jp/creep/index_en.html
35. Pitkänen H, Alatalo M, Puisto A, Ropo M, Kokko K, Vitos L (2013) Ab initio study of the surface properties of austenitic stainless steel alloys. Surf Sci 609:190–194. doi:10.1016/j.susc.2012.12.007
36. AHV (1991) Properties and selection: nonferrous alloys and special-purpose materials, vol 2. ASM International, Materials Park
37. Park D-B, Huh M-Y, Jung W-S, Suh J-Y, Shim J-H, Lee S-C (2013) Effect of vanadium addition on the creep resistance of 18Cr9Ni3CuNbN austenitic stainless heat resistant steel. J Alloy Compd 574:532–538. doi:10.1016/j.jallcom.2013.05.106
38. Vujic S, Sandström R, Sommitsch C (2015) Precipitation evolution and creep strength modelling of 25Cr20NiNbN austenitic steel. Mater High Temp. doi:10.1179/1878641315Y.0000000007
39. Sandström R, Wu R, Hagström J (2015) Grain boundary sliding in copper and its relation to cavity formation during creep. Mater Sci Eng. doi:10.1016/j.msea.2015.10.100